J. metamorphic Geol., 2000, **18,** 665–681

High-precision geothermobarometry across the High Himalayan metamorphic sequence, Langtang Valley, Nepal

G. FRASER,[1*] B. WORLEY[2] AND M. SANDIFORD[2]
[1]*Department of Geology and Geophysics, The University of Adelaide, South Australia, 5005, Australia (fraser@geo.ucalgary.ca)*
[2]*School of Earth Sciences, The University of Melbourne, Victoria, 3052, Australia*

ABSTRACT One of the long recognized features of Himalayan geology is the apparent inversion of metamorphic sequences, as evidenced in both metamorphic parageneses and thermobarometric data. With the aid of an extended thermobarometric dataset from the Langtang Valley section of the Higher Himalayan Crystallines, it can be demonstrated that the relatively large uncertainties associated with traditional thermobarometric techniques severely limit the tectonic interpretation of metamorphic gradients across the Himalayas. We apply the recently developed ΔPT approach, which significantly improves the precision to which pressure and temperature *differences* between samples may be calculated. High-precision thermobarometric data reveal an isothermal, rather than inverted, temperature array at Langtang, while the pressure data suggest significant structural complexity, with the Higher Himalayan Crystallines in the Langtang section comprising two distinct, possibly duplicated sequences, each having experienced considerable structural attenuation following metamorphism.

Key words: geothermobarometry; Himalayas; inverted metamorphism; Langtang.

INTRODUCTION

Geothermobarometry is commonly used by metamorphic geologists for reconstructing the geological history of individual samples and entire terranes, with the ultimate aim of constraining tectonic processes. Various sources of uncertainty contribute to the final uncertainties in thermobarometric calculations, limiting the eventual utility of the results as discriminants between potential tectonic scenarios. These sources of uncertainty can be broadly separated into geological errors, arising from input uncertainty, and computational errors, arising during pressure and temperature calculations. A recently developed geothermobarometric method, the ΔPT approach (Worley & Powell, 2000), significantly improves the precision on calculated differences in pressure and temperature, making it particularly applicable to problems where spatial variations or gradients are of more interest than absolute values of P and T. Here we apply the ΔPT approach to rocks from the Langtang Valley in the Nepalese Himalayas, to constrain P–T field gradients across a crustal section of *c.* 15 km. The application of the ΔPT approach to the Langtang section reveals details in the baric structure of this section that have been obscured in previous studies by large uncertainties in absolute pressure estimations. The results are discussed in the context of alternative models for the origin of apparent 'inverted' metamorphic gradients in the Himalayas.

*Present address: Department of Geology and Geophysics, University of Calgary, Calgary, Alberta, T2N 1N4, Canada. (fraser@geo.ucalgary.ca)

INVERTED METAMORPHIC P–T ARRAYS IN THE HIMALAYAS

It has long been recognized that the metamorphic grade of rocks on the southern side of the Himalayas increases from south to north and that, together with the north-dipping setting, this represents an apparent increase in metamorphic temperature up the structural section. This apparent inversion of the normal geothermal structure has been the subject of numerous studies, based on observations (e.g. Hubbard, 1989, 1996; Inger & Harris, 1992; Metcalfe, 1993; Macfarlane, 1995; Vannay *et al.*, 1999) and on theoretical considerations (e.g. Jaupart & Provost, 1985; England & Molnar, 1993; Ruppel & Hodges, 1994; Jamieson *et al.*, 1996). In detail, two apparent inverted metamorphic sequences have been recognized in the Himalayas. The first is across the Main Central Thrust (MCT), where kyanite-bearing rocks structurally overlie chlorite-grade Lesser Himalayan metasedimentary rocks, and the second is found within the hanging wall of the MCT, where kyanite-bearing rocks are overlain by sillimanite-bearing rocks. A variety of causative processes have been proposed for the inversion of metamorphic gradients in the Himalayas, including post-metamorphic deformation (e.g. Hubbard, 1996), synmetamorphic thrusting accompanied by shear heating (e.g. England & Molnar, 1993), decompression melting and the emplacement of leucogranites during

exhumation (e.g. Inger & Harris, 1992; Davidson *et al*., 1997), and heat focusing below low-conductivity sediments (Jaupart & Provost, 1985). While these hypotheses are based on a combination of structural, metamorphic and geochronological observations, one of the fundamental lines of evidence is the spatial variation of metamorphic pressure and temperature across the region.

Before turning to the thermal and baric structure of the Langtang section of the Higher Himalayas, it is worth briefly considering the tectonic implications of the preserved pressure array within a crustal section. A lithostatic pressure gradient is to be expected in a case where all samples equilibrated synchronously within a section which has not subsequently been structurally disrupted. In contrast, diachronous metamorphic equilibration within a section, during *P*–*T*–time evolution, will produce pressure arrays which deviate from lithostatic, as will post-metamorphic structural disruption of the section. The preserved pressure array therefore potentially provides an insight both into processes governing metamorphism and the extent of subsequent structural activity. To illustrate causes of a non-lithostatic preserved pressure gradient, let us first consider the case of an exhuming crustal block, with all rocks undergoing clockwise *P*–*T*–time paths (e.g. England & Thompson, 1984). Peak temperatures will be reached at progressively later times with increasing depth, and the apparent barometric gradient preserved by the array of pressures at peak temperature (P_{Tmax}) will be less than the expected lithostatic gradient for the appropriate average density over the depth range of interest. This effect is largely a consequence of the role played by the Earth's surface, which has a most pronounced effect at shallow levels. The result is that shallower rocks will tend to reach peak temperatures at a depth close to their maximum depth, whereas deeper rocks will continue to heat for a larger proportion of their exhumation path, reaching peak temperatures at significantly shallower levels than their maximum depth. The net effect is a preserved metamorphic pressure gradient less than lithostatic. The reduction of the preserved pressure gradient in this case is related to the rate of exhumation of the crustal section, and parameters such as the thermal conductivity and internal heat production. Homogeneous thickening of a section subsequent to metamorphic equilibration will also reduce the preserved pressure gradient by increasing the structural distance between rocks which metamorphically equilibrated closer together. In contrast, apparent pressure gradients that are steeper than lithostatic are expected to result from structural extension subsequent to metamorphic equilibration. It should be noted, however, that Jamieson *et al*. (1996) showed that steeper than lithostatic apparent pressure arrays can also be produced by a model involving synmetamorphic ductile shear, depending on the convergence rate and exhumation rate. Jamieson *et al*. (1996) also make the point that an apparently lithostatic pressure array can be produced in exposed rocks even though the points that define it never formed a vertical array. Thus, the appearance of a lithostatic pressure array does not necessarily imply structural coherence.

The discussion above illustrates that, in principle, preserved metamorphic temperature and pressure arrays may provide valuable constraints on tectonic reconstructions. In practice, however, relatively large uncertainties on individual temperature and pressure estimates severely limit the utility of trends in the data as a tectonic tool. For example, Macfarlane (1995) noted that deviation from a lithostatic gradient, due to equilibration at different times up-section during exhumation at realistic rates, is unlikely to be detected using traditional thermobarometric techniques. In this contribution, we re-examine the distribution of calculated metamorphic pressure and temperature conditions within the hanging wall of the MCT, across the Langtang Valley section of the Higher Himalayas. We build on the previous work of Inger & Harris (1992) and Macfarlane (1995) and present high-precision geothermobarometric results using the approach of Worley & Powell (2000).

GEOLOGICAL SETTING OF THE LANGTANG VALLEY

The geological structure of the Himalayan orogen can be broadly divided into three east–west-trending zones, separated by major north-dipping faults (Fig. 1). At the southern margin of the orogen, the Main Boundary Thrust (MBT) juxtaposes molassic sediments of the Siwalik foreland with the low-grade metasedimentary rocks of the Lesser Himalayan sequence. To the north, across the MCT, the main divide of the Himalayan range is composed of the Higher Himalayan Crystallines (HHC), which structurally overlie the Lesser Himalayan sequence. Still further north,

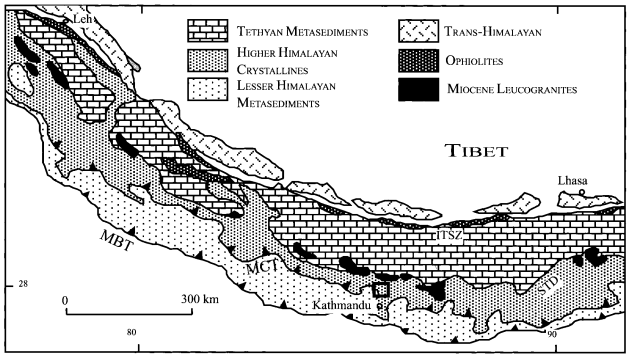

Fig. 1. Generalized geological map of the Himalayas showing the major lithological and structural features. MBT, Main Boundary Thrust; MCT, Main Central Thrust; STD, South Tibetan Detachment; ITSZ, Indus Tsangpo Suture Zone. The box north of Kathmandu shows the position of the Langtang Valley.

the HHC are truncated by a major normal fault system, the South Tibetan Detachment (STD), north of which lies the Tibetan sedimentary sequence.

The Langtang Valley is situated *c.* 75 km north of Kathmandu in central Nepal (Fig. 1), and drains south-westward from the High Himalayan divide, which forms the border between Nepal and Tibet. The valley cuts across the strike of north-east-dipping metasedimentary rocks exposing approximately 20 km of structural thickness through the HHC (Fig. 2). The base of the Langtang section, near the junction of the Langtang and Trisuli Rivers, exposes the MCT zone, a broad (*c.* 4 km thick) region of ductile shear which juxtaposes chlorite- and biotite-grade Lesser Himalayan metasedimentary rocks with amphibolite facies metasedimentary rocks of the HHC. The lowermost *c.* 5 km of the HHC in the Langtang Valley contains kyanite-bearing metapelitic assemblages, whereas structurally higher in the section fibrolitic sillimanite is common. The upper part of the Langtang HHC sequence contains large volumes of post-kinematic leucogranite, forming sills and sheets subconcordant to regional schistosity, which can be divided into a tourmaline-bearing suite and a two-mica-bearing suite (Inger & Harris, 1993). These sills and sheets appear to have been fed by dykes which cross-cut schists and gneisses immediately below the level of emplacement.

The protolith of the HHC at Langtang is regarded as late Proterozoic clastic sediment, based on detrital zircon ages between 1.0 and 0.8 Ga (Parrish & Hodges, 1996). Uranium–lead ages of accessory minerals show no evidence for pre-Himalayan or Eo-Himalayan metamorphism, with monazite yielding early to mid-Miocene ages (Parrish & Hodges, 1996), interpreted to approximate the time of peak metamorphism. On the basis of $^{40}Ar/^{39}Ar$ ages for biotite, Macfarlane (1993) concluded that peak metamorphism occurred between 22 and 19 Ma, with rapid cooling of the upper part of the section recorded by $^{40}Ar/^{39}Ar$ biotite ages of around 19 Ma, while slower cooling of the lower section resulted in biotite closure to argon diffusion between 10 and 5 Ma. Macfarlane (1995) suggested

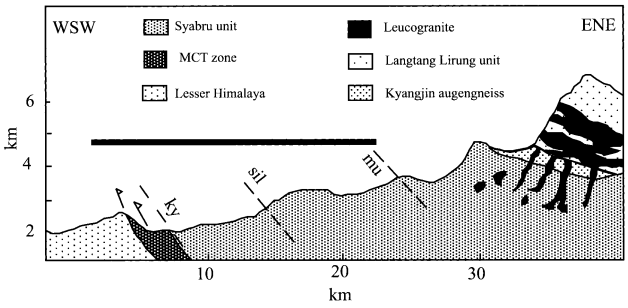

Fig. 2. Geological cross-section up the Langtang Valley (modified from Inger & Harris, 1992). The black bar shows the region over which samples were collected for geothermobarometry.

two periods of movement on the MCT, the first being early ductile movement which was synchronous with metamorphism, occurring before *c.* 6 Ma, followed by brittle movement at *c.* 2.3 Ma. Inger & Harris (1992) presented Rb–Sr mica ages from Langtang, which they interpreted to indicate cooling of the upper part of the HHC section through *c.* 350 °C by about 17 Ma, while cooling of the lower part of the section did not occur until *c.* 5 Ma, in accord with the interpretation of Macfarlane (1993).

PREVIOUS GEOTHERMOBAROMETRY

Two previous studies have presented thermobarometric data from the Langtang Valley. Inger & Harris (1992) used THERMOCALC (Powell & Holland, 1988) and the internally consistent thermodynamic dataset of Holland & Powell (1990) to produce pressure and temperature profiles across the lower *c.* 15 km of the HHC, based on results from 14 samples. Although their data showed considerable scatter, Inger & Harris (1992) noted that metamorphic temperatures were within a range of *c.* 150 °C, at around 700 °C, implying either a relatively low geothermal gradient within the section, or diachronous equilibration. Pressure estimates from the top of the section were significantly lower than those from the base of the section and, although the data were scattered, Inger & Harris (1992) proposed two populations in the pressure data, which they attributed to diachronous metamorphism between the kyanite and sillimanite zones.

In a similar study, Macfarlane (1995) calculated *P–T* conditions from 19 samples using simultaneous solution of the garnet–biotite thermometer (Ferry & Spear, 1978) and either the garnet–muscovite–biotite–plagioclase barometer (Ghent & Stout, 1981) or the garnet–aluminosilicate–quartz–plagioclase barometer (Ghent, 1976). Results from the same 15 km section as that sampled by Inger & Harris (1992) showed metamorphic temperatures within uncertainty of 605 °C throughout, and a metamorphic pressure gradient consistent with an average crustal lithostatic gradient of *c.* 27 MPa km^{-1}.

Results from these previous studies have led to contrasting interpretations of the metamorphic history of the HHC at Langtang. Inger & Harris (1992) suggested that, although the HHC represents a coherent crustal block, sillimanite-zone rocks resulted from overprinting of existing kyanite-bearing rocks during a distinct thermal event, associated with the emplacement of leucogranites at the top of the HHC section. This interpretation was based on their barometric data, in which pressures calculated from sillimanite-zone rocks plotted as a group at lower pressures than kyanite-zone rocks. Their data coverage, however, was sparse, particularly across the kyanite to sillimanite transition zone. Inger & Harris (1992) supported their argument for polymetamorphism in the sillimanite zone with the observation of kyanite inclusions within

garnet in sillimanite-bearing rocks, although it is equally possible that this texture could result from progressive metamorphism at increasing temperature or decreasing pressure during a 'single' metamorphic event.

Macfarlane (1995) interpreted the pressure array revealed by her data as indicating the HHC to be a coherent structural block, based on the apparently continuous trend of decreasing pressure up the section. Macfarlane (1995) noted that, within the error of her data, the pressure array can be explained by cooling throughout the HHC block in response to exhumation, provided that adjacent units cooled within a few million years of each other. This explanation therefore does not require distinct thermal events or tectonic juxtaposition to account for the kyanite- and sillimanite-zone metamorphism.

Reddy *et al.* (1993) did not present *P–T* data, but argued for a structural break between the kyanite and sillimanite zones based on textural observations. Reddy *et al.* (1993) regarded kyanite growth to be post-kinematic and sillimanite growth to be syn-kinematic. They therefore suggested that foliation development in the kyanite zone pre-dated MCT movement, and represented a pre- or early Himalayan fabric unrelated to MCT movement, whereas foliation development in the sillimanite zone was associated with later top to the south-west thrust emplacement of the sillimanite zone onto the kyanite zone. The possibility still exists, however, that foliation development throughout the section was related to top to the south-west thrusting associated with early MCT movement, but that deformation migrated vertically through the section allowing kyanite growth to outlast deformation in the lower part of the section. Reddy *et al.* (1993) also cited contrasting strontium and oxygen isotope signatures in the kyanite versus sillimanite zones to support the argument for tectonic juxtaposition.

In both previous thermobarometric studies at Langtang, 2σ uncertainties on the calculated *P–T* results are on the order of ± 200 MPa and ± 100 °C, allowing for only very general trends to be distinguished. Neither study had the benefit of X-ray mapping to distinguish internal compositional variation in garnet, although in both cases mineral compositions measured near grain margins were used in the thermobarometric calculations. On the basis of electron probe microanalysis compositional profiles, Inger & Harris (1992) regarded compositional zonation in garnet to be rare, in contrast to the results of our X-ray mapping in which zonation is almost ubiquitous (see below). Macfarlane (1995) recognized distinct garnet zonation in Lesser Himalayan and lower MCT-zone samples, similar to that seen in samples LG39 and LG40 presented below, but less extreme zonation in upper MCT-zone and HHC samples.

In the next section, we present thermobarometric results from several new samples. These results are combined with recalculated *P–T* estimates using the published mineral composition data of both Inger & Harris (1992) and Macfarlane (1995) to produce a more comprehensive and internally consistent *P–T* dataset for the Langtang Valley.

PETROGRAPHY

The work presented here focuses on samples collected from across the lowermost *c.* 15 km of the HHC section at Langtang, spanning the kyanite and fibrolitic sillimanite zones, and including samples from the MCT zone at the base of the section (Fig. 3). All samples come from the Syabru Unit of Reddy *et al.* (1993). This part of the section is dominated by foliated pelitic and semipelitic schists with an average dip of approximately 45° to the NE, subparallel to the orientation of the MCT. Most structural models for this part of the Himalaya imply that the present orientation of the foliation is due to ramping on the upper part of the MCT which flattens with depth to form part of the Main Himalayan Thrust decollement (Brown *et al.*, 1996). Based on the assumption that, at the time of metamorphism, the foliation was probably close to horizontal, relative structural heights have been calculated for samples used in the geothermobarometric calculations presented below.

The typical assemblage in HHC rocks from Langtang is biotite–garnet–muscovite–plagioclase–quartz ± aluminosilicate. Garnet occurs as porphyroblasts up to about 1 cm, but more typically about 1–3 mm, in diameter (Fig. 4). Porphyroblasts from both the kyanite and sillimanite zones contain inclusions of quartz + biotite ± rutile, which commonly define spiral or sigmoidal trails indicative of early garnet growth synchronous with deformation. The exterior of garnet porphyroblasts is generally inclusion-free, and appears to post-date the development of the dominant mica fabric. Garnet also occurs as small inclusion-free grains which appear to post-date biotite and muscovite fabric development (Fig. 4c). Garnet is almandine-rich, with minor but variable pyrope, grossular and spessartine components, discussed in more detail below. Kyanite is the stable aluminosilicate phase in the lower *c.* 5 km of the HHC section, and makes up to several modal per cent of some samples. In micaceous bands, it occurs as large euhedral grains weakly aligned within the mica foliation (Fig. 4b), whereas it is commonly randomly oriented in quartz-rich domains. Elongate kyanite does not form a mineral lineation, but is randomly oriented within foliation planes, suggesting post-kinematic growth. Macfarlane (1995) and Inger & Harris (1992) reported kyanite inclusions within garnet in some samples. Sillimanite occurs only in samples from the upper part of the section, initially appearing about 5 km above the MCT zone. It occurs as fibrolitic bundles generally aligned in the main foliation, although in some rocks it appears randomly oriented. Macfarlane (1995) reported coexisting kyanite and sillimanite in some samples from the boundary between the kyanite and sillimanite zones. Muscovite occurs in most samples, but is most abundant in the lower part of the HHC section, where it defines the regional foliation. In the sillimanite zone, a second generation of muscovite appears to overgrow both fibrolite and the regional foliation. Biotite is common to all samples and defines the regional foliation. Staurolite was found only in one sample (LG36), where it occurs as anhedral grains in the matrix together with kyanite, garnet, biotite and muscovite. Inger & Harris (1992) also reported staurolite inclusions in garnet from one sample in the sillimanite zone. Albitic plagioclase (Ab generally >70 mol.%) occurs as a matrix phase together with quartz, and makes up 5–20 modal per cent of most samples. Chloritoid was found in two samples (LG39, LG40) from the lower part of the MCT zone north of the town of SyabruBensi (Fig. 3). It occurs as large elongate grains oriented parallel to a muscovite–biotite foliation.

Differing interpretations of the metamorphic history of the HHC have been proposed by previous workers based on fabric relationships. Much of the difference in opinion is due to assumptions, explicit or implicit, that either metamorphism or fabric development was synchronous up the section. In principle, very detailed geochronology which revealed the age of 'peak' metamorphism, or the time of fabric development, could allow testing of these

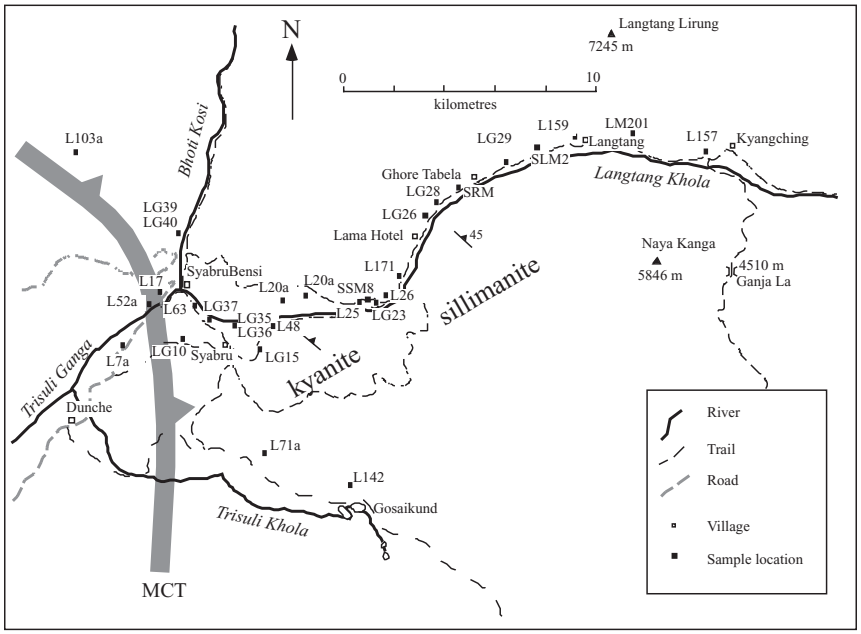

Fig. 3. Map of the Langtang region showing sample localities. The grey band north-east of the MCT marks the boundary between the kyanite and sillimanite zones.

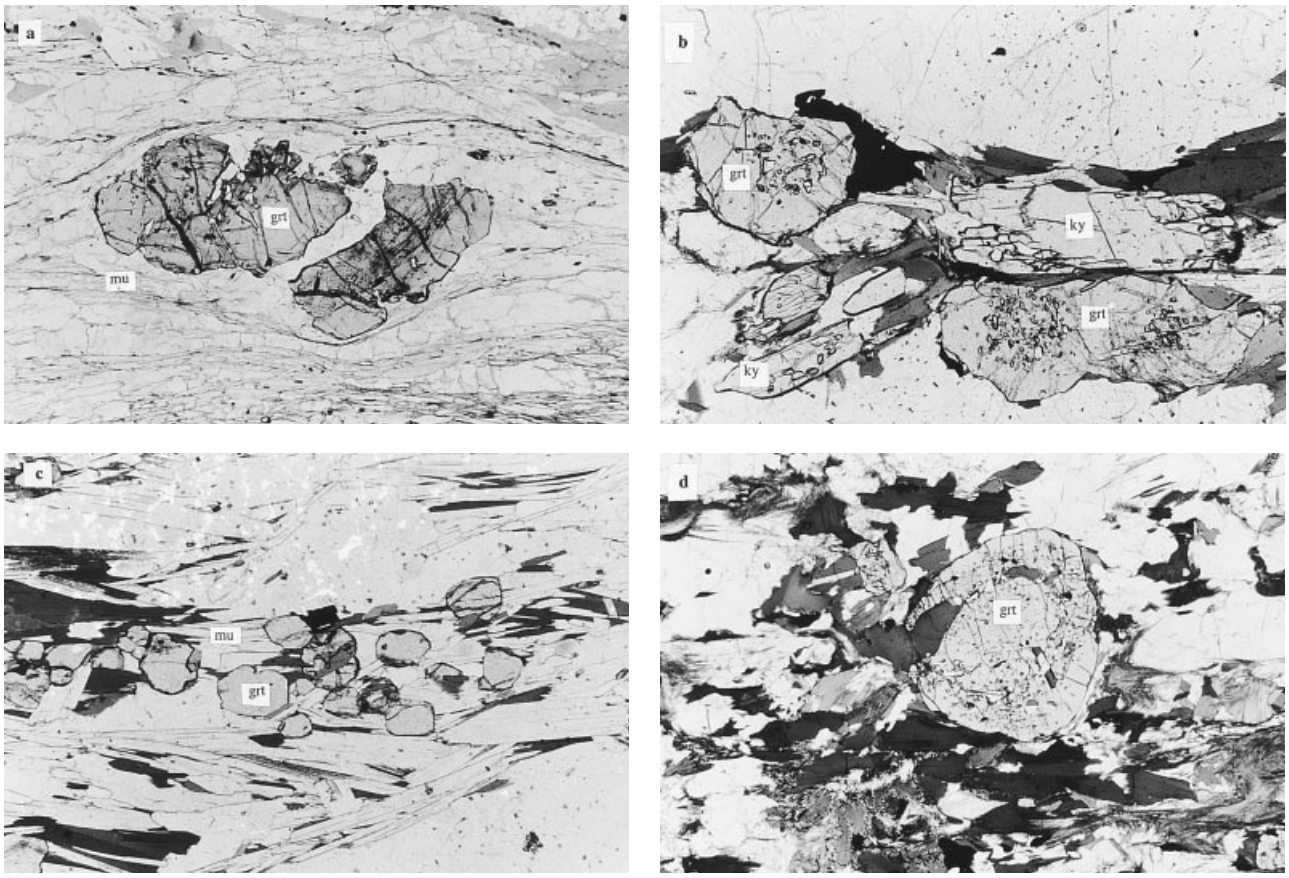

Fig. 4. Photomicrographs illustrating porphyroblast fabric relationships. (a) LG 40: MCT zone. Fractured garnet porphyroblast wrapped by a muscovite foliation, illustrating post-metamorphic deformation within the MCT zone. Long dimension of photograph is 1 cm. (b) LG35: kyanite zone. Garnet (upper left and lower right) and kyanite (tabular grains, centre right and lower left) porphyroblasts overgrowing biotite–muscovite foliation. Long dimension of photograph is 0.5 cm. (c) LG36: kyanite zone. Garnet overgrowing muscovite–biotite foliation. Long dimension of photograph is 0.5 cm. (d) LG23: sillimanite zone. Garnet porphyroblast with inclusion-free rim overgrowing biotite foliation. This sample also contains abundant fibrolitic sillimanite, occurring both within the biotite foliation and as randomly oriented needles. Long dimension of photograph is 1 cm.

assumptions. However, the current state of geochronology is probably not at a level where this could be achieved with sufficient resolution. Without making these assumptions, only the following general implications can be drawn from the mineral textures. Textural relationships, in which garnet, kyanite and, in some cases, sillimanite appear to post-date the main mica foliation at Langtang, suggest that near-peak metamorphism outlasted deformation in the HHC throughout the Langtang section. As pointed out by Reddy *et al.* (1993), since movement on the MCT juxtaposes the HHC above lower grade Lesser Himalayan rocks, final movement on the MCT must post-date fabric development in the HHC. This does not, however, rule out the possibility of early MCT movement related to fabric development in the HHC. The observation that the dominant foliation in the HHC is subparallel to the MCT is consistent with, but does not require, foliation development associated with MCT movement.

X-RAY MAPPING

Intragrain garnet compositional variation has been documented via semiquantitative X-ray maps. This has been undertaken for each sample, enabling informed selection of sites for quantitative electron probe microanalyses to be used in thermobarometric calculations. X-Ray maps were collected using the Cameca SX-51 electron probe at The University of Adelaide, at operating conditions of 15 kV and either 500 or 1000 nA, with a dwell time of 10 ms. The instrument has four crystal spectrometers, which were configured for simultaneous counting of Ca, Fe, Mn and Al or Mg.

Representative X-ray maps of garnet are shown in Fig. 5. Typical zonation patterns show a decrease in Ca and Mg and an increase in Mn content from core to rim. The Fe zonation is generally weak, but most commonly increases towards the rim. Sample LG35 is an exception to these general trends, with Ca zonation exhibiting a euhedral interior region with relatively low Ca content, surrounded by an embayed outer zone which shows the typical zonation of decreasing Ca towards the rim. In many cases, zonation patterns are not centred in the grain, and do not necessarily mimic the shape of the grain outline (e.g. Fig. 5, LG15, LG31).

It is important to distinguish the origin of the compositional zonation in order to choose appropriate mineral compositions for thermobarometric calculations and, furthermore, to correctly interpret the resulting *P–T* estimations. Several lines of evidence suggest that the zonation patterns observed in garnet from the HHC are most likely the result of diffusional re-equilibration, rather than growth zoning. First, the characteristic pattern of increasing Mn content at garnet rims contrasts with the bell-shaped Mn profiles commonly attributed to growth zonation. In addition, steep zonation in HHC garnet is restricted to a relatively narrow zone at grain margins, and in some grains around large inclusions of quartz (e.g. Fig. 5, LG15), suggesting diffusion acting from the grain boundary subsequent to growth. Some garnet (e.g. Fig. 5, LG31) shows zonation patterns which mimic deep embayments. Assuming that the embayments are resorption features rather than primary growth features implies that the characteristic zonation in HHC garnet is due to diffusional re-equilibration. Since diffusion of major element cations in garnet is negligible at temperatures below about 500 °C (e.g. Spear, 1993), the zonation in HHC garnet is likely to reflect re-equilibration at near-peak metamorphic conditions.

Two samples (LG39, LG40) from the basal part of the MCT zone, collected from the Bhoti Khosi north of the town of SyabruBensi, show distinctly different zonation patterns in garnet, characterized by a sharply defined euhedral core with higher Ca content (Fig. 5). Zonation in Fe, Mg and Mn is also evident, but is considerably more diffuse than Ca zonation. This zonation is similar to that documented in Lesser Himalayan garnet by Macfarlane (1995) using compositional profiles. Both LG39 and LG40 contain chloritoid which distinguishes them from other samples collected in this study. Chloritoid has an upper stability limit of less than 600 °C between 500 and 1000 MPa (e.g. Mahar *et al.*, 1997), significantly less than temperature estimates derived from other HHC samples (see below). These two samples are therefore interpreted to represent a sliver of the Lesser Himalayan sequence which was tectonically incorporated into the MCT zone during thrust movement. The sharp zonation within garnet in these two samples is interpreted as a growth feature, as it occurs in a narrow zone in the interior of grains, rather than at grain boundaries, and the Ca zonation, in particular, is distinctly euhedral. The abrupt change in garnet composition within these samples suggests two distinct garnet growth episodes in these rocks, although whether these correspond to distinct tectonic events or to different portions of a single *P–T* path is unclear. One possibility is that the growth of garnet rims in these samples is related to emplacement of the HHC above the Lesser Himalayan sequence, via movement on the MCT subsequent to metamorphism in the HHC, whereas the high-Ca garnet cores represent an earlier metamorphic episode within the Lesser Himalayan sequence. This interpretation is consistent with recent geochronological results from the Lesser Himalaya in the region immediately west of Langtang, indicating peak metamorphism in the MCT footwall at about 6 Ma (Harrison *et al.*, 1997). Without detailed comparative geochronology, the correlation of metamorphism in the HHC with the growth of garnet cores in the footwall of the MCT remains speculative.

GEOTHERMOBAROMETRY RESULTS

The X-ray mapping illustrates considerable internal zonation in garnet compositions, raising questions about which compositions are appropriate for thermobarometric calculations. We have selected regions within both core and rim domains in garnet for use in thermobarometric calculations. The mineral compositions are given in Table 1. All thermobarometric calculations have been made using THERMOCALC v.3 (Powell & Holland, 1988), and the latest version

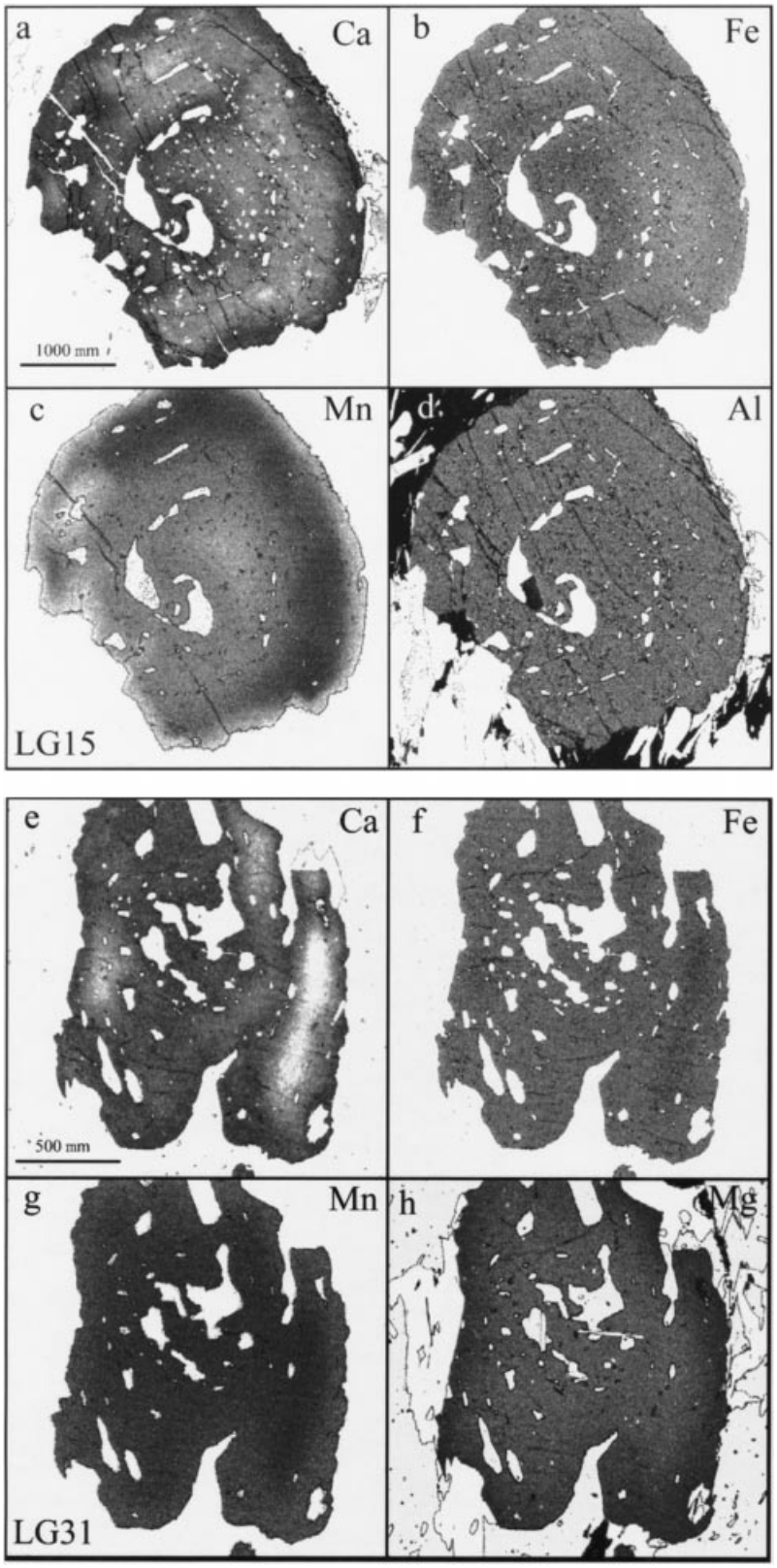

Fig. 5. Representative X-ray maps of garnet compositions: (a–d) sample LG15: kyanite zone; (e–h) sample LG31: sillimanite zone; (i–l) sample LG35: kyanite zone; (m–p) sample LG40: MCT zone. The poorer resolution of the maps of sample LG35 results from collecting over a grid of 256×256 pixels, whereas all other maps comprise 512×512 pixels. In every case, lighter tones indicate higher concentrations of the element analysed.

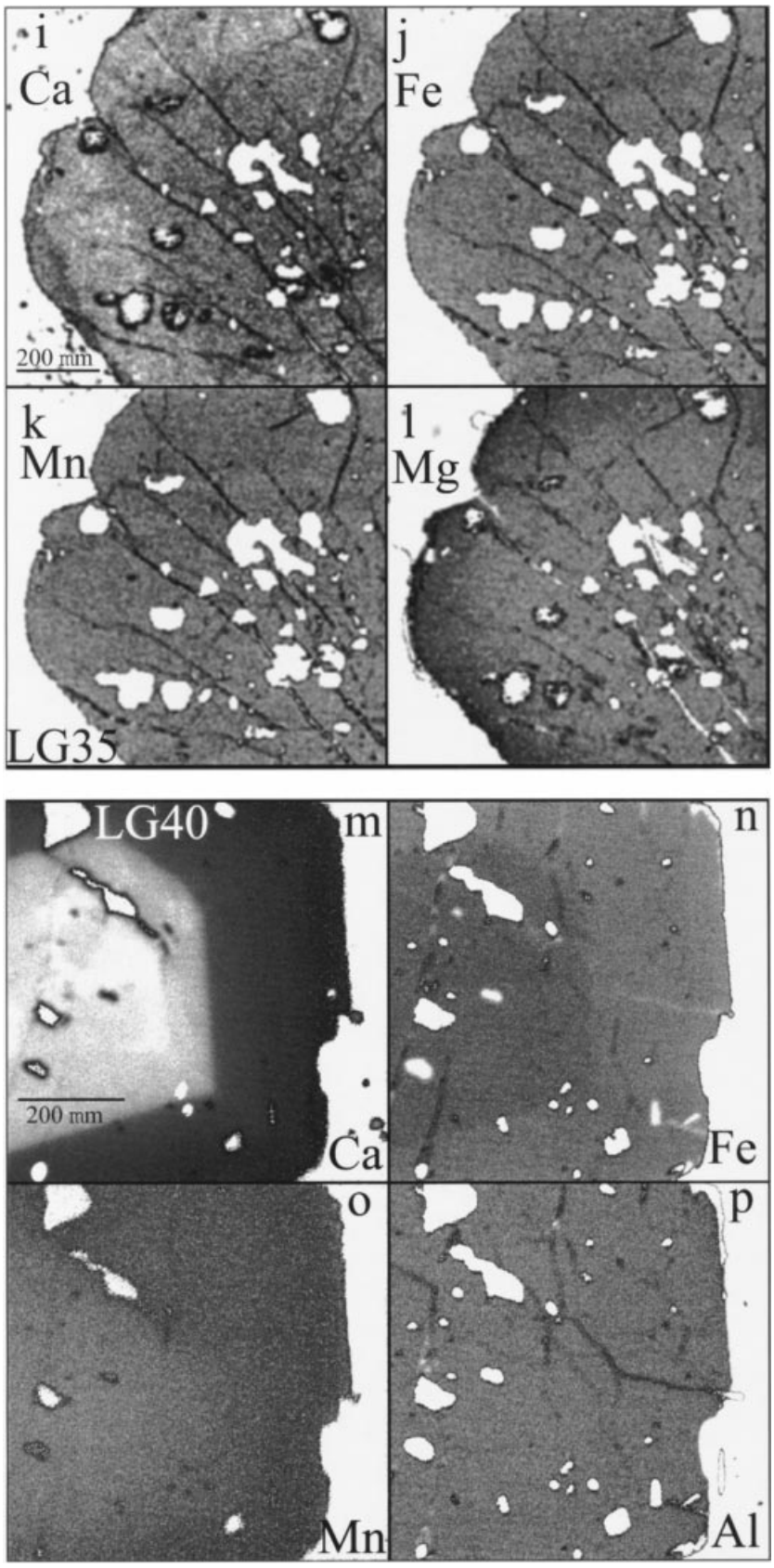

Fig. 5. *Continued.*

Table 1. Representative electron probe microanalyses of minerals used for thermobarometry.

	LG10			LG15					LG23					LG26				
	g	bi	pl	g (r)	g (c)	bi	mu	pl	g (r)	g (c)	bi	mu	pl	g (r)	g (c)	bi	mu	pl
SiO_2	37.27	35.96	64.08	37.83	38.03	37.11	47.62	61.56	37.22	37.58	35.29	47.80	62.21	36.58	37.07	34.32	45.72	63.89
TiO_2	0.05	2.31	0.02	0.20	0.00	1.98	0.59	0.00	0.06	0.00	3.23	0.76	0.01	0.04	0.00	3.84	1.08	0.00
Al_2O_3	21.23	17.55	21.56	21.33	21.47	18.48	35.01	24.09	20.92	21.05	19.21	36.30	23.77	20.52	20.93	18.84	33.75	22.18
FeO	32.17	16.87	0.00	29.36	29.09	15.31	1.61	0.02	32.17	32.53	19.68	0.98	0.00	33.78	32.52	20.04	0.00	0.00
MnO	3.46	0.01	0.02	2.93	1.35	0.09	0.03	0.07	6.28	3.43	0.16	0.00	0.03	3.51	2.66	0.05	1.27	0.00
MgO	4.70	11.8	0.00	4.29	5.20	13.25	1.09	0.00	2.36	3.58	8.51	0.67	0.00	2.49	3.28	7.46	0.03	0.00
CaO	1.63	0.11	3.04	3.44	4.49	0.01	0.01	5.38	1.16	1.81	0.00	0.00	5.13	1.49	2.39	0.00	0.84	4.01
Na_2O	0.08	0.38	9.50	0.00	0.00	0.35	0.94	8.16	0.00	0.01	0.14	0.51	8.29	0.00	0.03	0.13	0.00	9.19
K_2O	0.00	8.86	0.14	0.00	0.00	9.51	9.94	0.13	0.03	0.00	9.32	10.60	0.29	0.00	0.02	9.73	0.45	0.31
Total	100.59	93.85	98.36	99.20	100.38	96.10	96.85	99.41	100.20	99.99	95.55	97.63	99.73	98.78	99.02	94.51	100.94	99.58
O	12	11	8	12	12	11	11	8	12	12	11	11	8	12	12	11	11	8
Si	2.95	2.74	2.87	3.02	2.99	2.74	3.11	2.74	3.01	3.01	2.68	3.09	2.76	3.00	3.00	2.66	3.09	2.83
Ti	0.00	0.13	0.00	0.00	0.00	0.11	0.03	0.00	0.00	0.00	0.19	0.04	0.00	0.00	0.00	0.22	0.06	0.00
Al	1.98	1.58	1.14	2.01	1.99	1.61	2.70	1.27	1.99	1.99	1.72	2.77	1.24	1.98	2.00	1.72	2.69	1.16
Fe^{3+}	0.13	0.00	0.00	0.00	0.04	0.00	0.00	0.00	0.00	0.00	0.00	0.00	0.00	0.02	0.01	0.00	0.00	0.00
Fe^{2+}	2.00	1.08	0.00	1.96	1.91	0.65	0.09	0.00	2.17	2.18	1.25	0.05	0.00	2.32	2.20	1.30	0.72	0.00
Mn	0.23	0.00	0.00	0.20	0.09	0.01	0.00	0.00	0.43	0.23	0.01	0.00	0.01	0.24	0.18	0.00	0.00	0.00
Mg	0.55	1.34	0.00	0.51	0.61	1.46	0.11	0.00	0.28	0.43	0.96	0.07	0.00	0.30	0.40	0.86	0.09	0.00
Ca	0.14	0.01	0.15	0.29	0.38	0.00	0.00	0.26	0.10	0.16	0.00	0.00	0.24	0.13	0.21	0.00	0.00	0.19
Na	0.01	0.06	0.83	0.00	0.00	0.05	0.12	0.71	0.00	0.00	0.02	0.06	0.71	0.00	0.01	0.02	0.06	0.79
K	0.00	0.86	0.01	0.00	0.00	0.90	0.83	0.01	0.00	0.00	0.90	0.88	0.02	0.00	0.02	0.96	0.95	0.02
Total	8.00	7.80	5.00	7.98	8.00	7.53	6.99	4.98	7.99	8.00	7.74	6.96	4.98	8.0	8.00	7.75	7.01	4.99

	LG28					LG29					LG31				
	g (r)	g (c)	bi	mu	pl	g (r)	g(c)	bi	mu	pl	g (r)	g (c)	bi	mu	pl
SiO_2	36.69	36.69	33.87	44.87	64.85	35.95	36.76	34.05	47.15	59.98	36.53	37.11	33.43	46.79	54.19
TiO_2	0.01	0.01	3.56	0.95	0.01	0.01	0.02	2.51	0.56	0.00	0.07	0.00	3.64	0.31	0.00
Al_2O_3	20.70	20.70	18.22	34.13	21.69	20.59	20.48	19.13	35.62	25.00	20.56	20.44	18.65	35.95	28.06
FeO	32.64	32.64	21.59	1.52	0.02	34.65	35.44	23.41	1.40	0.00	35.21	35.41	24.09	1.31	0.00
MnO	4.27	4.27	0.13	0.00	0.00	2.70	2.31	0.08	0.00	0.00	1.77	1.23	0.05	0.00	0.03
MgO	2.80	2.80	7.03	0.77	0.00	2.03	2.10	5.85	0.52	0.00	1.99	1.89	5.10	0.46	0.00
CaO	1.38	1.38	0.00	0.00	3.27	1.47	1.84	0.10	0.00	7.04	2.26	3.27	0.00	0.00	11.05
Na_2O	0.02	0.02	0.14	0.60	9.55	0.01	0.02	0.14	0.46	7.84	0.05	0.01	0.11	0.39	5.43
K_2O	0.02	0.02	9.52	10.57	0.26	0.02	0.00	9.17	10.52	0.20	0.02	0.01	9.53	10.68	0.15
Total	99.50	99.50	94.07	93.42	99.64	98.49	99.08	94.48	96.27	100.1	99.32	99.37	94.61	95.92	99.14
O	12	12	11	11	8	12	12	11	11	8	12	12	11	11	8
Si	2.98	2.98	2.66	3.06	2.87	2.97	3.01	2.67	3.10	2.67	2.98	3.02	2.64	3.09	2.47
Ti	0.01	0.00	0.21	0.05	0.00	0.00	0.00	0.15	0.03	0.00	0.00	0.00	0.22	0.02	0.00
Al	1.98	1.98	1.69	2.74	1.13	2.00	1.98	1.77	2.76	1.31	1.98	1.96	1.74	2.80	1.51
Fe^{3+}	0.06	0.06	0.00	0.00	0.00	0.07	0.01	0.00	0.00	0.00	0.05	0.00	0.00	0.00	0.01
Fe^{2+}	2.22	2.22	1.42	0.09	0.00	2.39	2.43	1.54	0.08	0.00	2.41	2.41	1.59	0.07	0.00
Mn	0.29	0.29	0.01	0.00	0.00	0.19	0.16	0.01	0.00	0.00	0.12	0.09	0.00	0.00	0.00
Mg	0.34	0.34	0.82	0.08	0.00	0.25	0.26	0.68	0.05	0.00	0.24	0.23	0.60	0.05	0.00
Ca	0.12	0.12	0.00	0.00	0.16	0.13	0.16	0.01	0.00	0.34	0.20	0.29	0.00	0.00	0.54
Na	0.00	0.00	0.02	0.08	0.82	0.00	0.00	0.02	0.06	0.68	0.01	0.00	0.02	0.05	0.48
K	0.00	0.00	0.95	0.92	0.02	0.00	0.00	0.92	0.88	0.01	0.00	0.00	0.96	0.90	0.01
Total	8.00	8.00	7.78	7.02	4.99	8.00	8.00	7.77	6.96	5.01	8.00	8.00	7.77	6.97	5.02

of the Holland and Powell dataset (Holland & Powell, 1998). In addition to the new data for 10 samples, we have applied the THERMOCALC approach to the published mineral composition data from Inger & Harris (1992) and Macfarlane (1995) to improve the density of sample coverage in the Langtang section, resulting in a compiled *P–T* dataset of 29 samples across *c*. 15 km of structural section, all of which have been treated with a consistent geothermobarometric approach. It should be noted that Inger & Harris (1992) and Macfarlane (1995) presented only rim compositions for garnet, and so *P–T* calculations using garnet core compositions are limited to the additional samples collected in this study. Although a concerted attempt has been made in this study to account for compositional zonation, via the use of X-ray maps, there is no certainty that the grains we have analysed are cut through their centres. This may account for some of the scatter evident in the data calculated using garnet core compositions (Fig. 6). A strictly rigorous documentation of compositional zonation requires the recognition of the size and shape of grains in three dimensions, through techniques such as X-ray tomography (e.g. Denison *et al*., 1997). Despite the scatter, where core and rim compositions are available for the same sample, core compositions generally yield higher calculated values for both *P* and *T* than the rims (Fig. 6). However, only two cases (samples LG23, LG26) show very clear differences between core and rim *P–T* estimates, and, even in these cases, the estimates are within uncertainty. The remaining discussion will focus on results obtained using garnet rim

Table 1. (*Cont*.)

	LG35						LG36							LG37				
	g (r)	g (c)	bi	mu	pl	ilm	g (r)	g (c)	bi	mu	pl	st	ilm	g (r)	g (c)	bi	mu	pl
SiO_2	38.56	38.26	34.77	46.27	64.47	0.00	37.76	37.97	35.96	46.56	64.56	27.37	0.02	37.00	37.11	36.98	46.76	66.59
TiO_2	0.01	0.00	0.47	0.72	0.01	45.24	0.00	0.02	2.26	0.83	0.00	0.62	43.48	0.03	0.03	1.53	0.54	0.00
Al_2O_3	21.40	21.34	19.84	33.06	21.26	0.04	21.03	21.23	17.27	33.57	21.22	52.15	0.02	21.15	21.01	18.73	35.72	20.88
FeO	33.05	31.19	18.42	2.83	0.00	50.82	34.21	32.57	17.8	2.66	0.00	13.30	51.73	29.82	28.76	15.49	1.86	0.03
MnO	1.93	1.80	0.08	0.01	0.00	0.69	0.83	0.55	0.03	0.03	0.00	0.09	0.25	1.19	4.39	0.00	0.00	0.00
MgO	5.70	5.80	11.62	0.87	0.00	0.29	4.32	5.02	11.52	0.08	0.00	1.87	0.20	6.52	5.10	13.14	0.48	0.00
CaO	1.94	1.87	0.02	0.02	3.03	0.02	1.80	2.47	0.00	0.00	2.83	0.02	0.01	0.97	1.44	0.00	0.00	1.65
Na_2O	0.01	0.00	0.31	1.26	9.42	0.00	0.02	0.04	0.40	1.26	9.64	0.07	0.00	0.07	0.05	0.44	2.23	10.34
K_2O	0.01	0.00	9.29	9.35	0.12	0.00	0.00	0.00	9.00	9.45	0.10	0.00	0.01	0.02	0.01	8.79	7.77	0.06
Total	100.6	100.9	94.82	94.40	98.31	97.1	100.0	101.1	94.24	94.44	98.35	95.49	95.72	98.76	100.4	95.11	95.37	99.55
O	12	12	11	11	8	3	12	12	11	11	8	46	3	12	12	11	11	8
Si	3.02	3.00	2.63	3.12	2.88	0.00	3.01	2.98	2.75	3.14	2.88	7.77	0.00	2.95	2.94	2.75	3.08	2.93
Ti	0.00	0.00	0.03	0.04	0.00	0.88	0.00	0.00	0.13	0.04	0.00	0.13	0.85	0.00	0.00	0.09	0.03	0.00
Al	1.98	1.97	1.77	2.63	1.12	0.00	1.98	1.97	1.55	2.67	1.12	17.45	0.00	1.99	1.97	1.64	2.78	1.08
Fe^{3+}	0.00	0.04	0.18	0.00	0.00	0.24	0.00	0.07	0.00	0.00	0.00	0.00	0.29	0.12	0.15	0.00	0.00	0.00
Fe^{2+}	2.03	2.04	0.99	0.16	0.00	0.86	2.28	2.14	1.137	0.15	0.00	3.16	0.84	1.99	1.91	0.96	0.00	0.00
Mn	0.13	0.12	0.01	0.00	0.00	0.02	0.06	0.04	0.00	0.00	0.00	0.02	0.01	0.08	0.30	0.00	0.00	0.00
Mg	0.66	0.68	1.31	0.09	0.00	0.01	0.51	0.59	1.31	0.01	0.00	0.79	0.01	0.78	0.60	1.46	0.05	0.00
Ca	0.16	0.16	0.00	0.00	0.15	0.00	0.15	0.21	0.00	0.00	0.14	0.01	0.00	0.08	0.12	0.00	0.00	0.08
Na	0.00	0.00	0.05	0.17	0.82	0.00	0.00	0.01	0.00	0.17	0.84	0.04	0.00	0.01	0.01	0.06	0.29	0.88
K	0.00	0.00	0.90	0.81	0.01	0.00	0.00	0.00	0.00	0.81	0.01	0.00	0.00	0.00	0.00	0.84	0.65	0.003
Total	7.99	8.00	7.87	7.02	4.98	2.01	8.0	8.00	8.00	6.99	4.99	29.38	2.00	8.00	8.00	7.79	6.97	4.97

bi, biotite; g, garnet; ilm, ilmenite; mu, muscovite; pl, plagioclase; st, staurolite; c, core; r, rim.

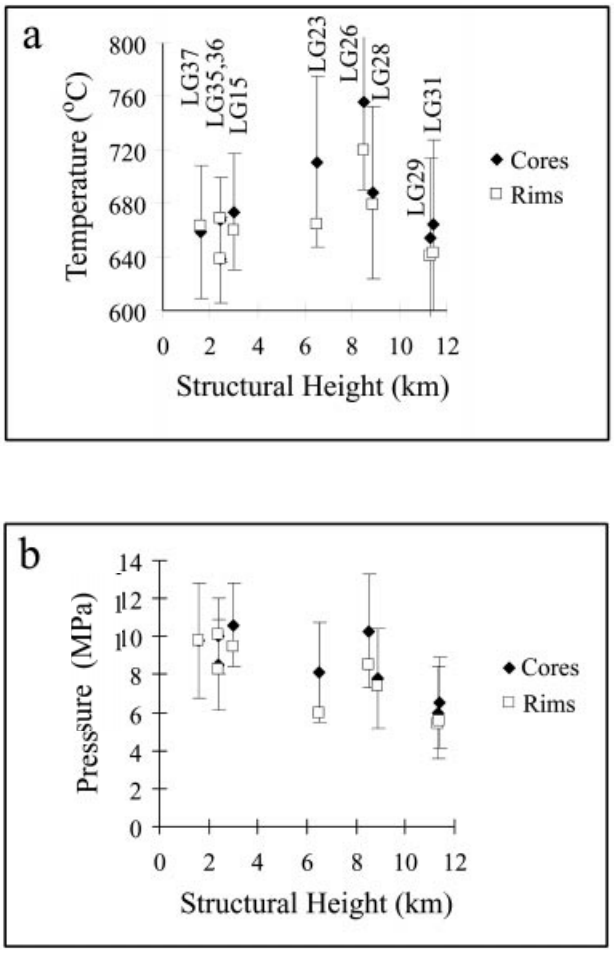

Fig. 6. Comparison of THERMOCALC average *P–T* results using garnet core and rim compositions.

compositions (Table 2), over which we have better spatial control, and which can more confidently be regarded as part of an equilibrium assemblage with the surrounding matrix phases.

Pressure and temperature estimates using garnet rim compositions are plotted against structural level in Fig. 7, where structural height has been calculated from geographic position assuming an average dip of 45° NE (Inger & Harris, 1992; Reddy *et al*., 1993; Macfarlane, 1995). The THERMOCALC results are broadly consistent with those of Macfarlane (1995), and appear to be considerably more systematic than the results of Inger & Harris (1992). Temperature estimates from within the HHC are essentially isothermal, with all samples across the *c*. 15 km of structural section plotting within error of 650 °C. There is no evidence in the *P–T* data for increasing temperature up-section within the HHC, although the samples do not extend to the uppermost levels of the section where leucogranites intrude. Samples from the MCT zone (samples L7a, L52a) yield slightly lower temperature estimates than those from the HHC, consistent with the previously documented inverted metamorphic field gradient across the MCT.

Calculated pressures decrease from around 900 MPa at the base of the HHC section to around 500 MPa 14 km structurally higher in the section, consistent with an average lithostatic gradient, as noted by Macfarlane (1995). Linear regression of the pressure data yields an average gradient of 30 ± 8 MPa km^{-1}, well within error of an average lithostatic gradient of *c*. 27 MPa km^{-1} (assuming an average density of 2700 kg m^{-3}), but with considerable associated uncertainty. This is illustrated in Fig. 7, where pressure gradients 30% steeper and shallower than lithostatic have been plotted and also fall within error limits. The

Table 2. Results of THERMOCALC average *P–T* calculations from Langtang, using garnet rim and core compositions. All uncertainties are given at the 2σ level.

			Pressure (MPa)		Temperature (°C)	
Sample	Assemblage	Height above MCT (km)	Rims	Cores	Rims	Cores
MCT zone						
L7a	g–bi–mu–pl–chl–q–H_2O	−0.85	890±260		602±58	
L52a	g–bi–mu–pl–chl–q–H_2O	0.0	880±220		602±58	
Kyanite zone						
L17	g–bi–mu–pl–chl–q–H_2O	0.15	910±280		622±66	
LG10	g–bi–pl–ky–ru–q–H_2O	0.7	930±480		692±238	
L103a	g–bi–pl–ky–q–H_2O	1.0	890±400		574±194	
L63	g–bi–pl–mu–q–H_2O	1.3	950±240		627±60	
LG37	g–bi–mu–pl–ky–q–H_2O	1.6	980±300	980±300	663±50	659±50
LG35	g–bi–mu–pl–ky–ilm–ru–q–H_2O	2.4	1010±200	1000±200	669±32	668±32
LG36	g–bi–mu–pl–ky–ilm–st–q–H_2O	2.4	830±220	850±240	638±32	638±32
LG15	g–bi–mu–pl–ky–q–H_2O	3.0	950±220	1060±220	660±44	674±44
L71a	g–bi–pl–mu–ky–q–H_2O	3.0	820±220		641±44	
L48	g–bi–pl–mu–q–H_2O	3.4	910±280		646±74	
L20a	g–bi–pl–mu–q–H_2O	3.8	780±260		623±74	
L22	g–bi–pl–mu–ky–sill–q–H_2O	4.4	690±240		625±46	
L142	g–bi–pl–mu–q–H_2O	5.5	780±300		680±80	
L25	g–bi–pl–mu–ky–sill–q–H_2O	6.1	790±300		667±54	
SSM8	g–bi–mu–pl–ky–q–H_2O	6.4	930±360		763±82	
Sillimanite zone						
LG23	g–bi–mu–pl–sill–q–H_2O	6.5	600±260	810±260	664±64	711±64
L26	g–bi–pl–mu–sill–q–H_2O	6.8	690±280		651±66	
L171	g–bi–pl–mu–sill–q–H_2O	7.2	650±260		644±60	
LG26	g–bi–mu–pl–sill–q–H_2O	8.5	850±320	1030±300	720±76	756±66
LG28	g–bi–mu–pl–sill–q–H_2O	8.9	740±260	780±260	679±64	688±64
SRM4	g–bi–mu–pl–sill–q–H_2O	9.5	620±260		726±86	
LG29	g–bi–mu–pl–sill–q–H_2O	11.3	540±240	600±240	641±60	654±60
LG31	g–bi–mu–pl–sill–q–H_2O	11.4	560±240	650±240	643±64	664±64
SLM2	g–bi–Kfs–pl–sill–q–H_2O	12.0	770±1120		727±306	
L159	g–bi–pl–mu–sill–q–H_2O	13.4	450±320		640±60	
LM201	g–bi–Kfs–pl–sill–crd–q–H_2O	14.8	680±140		664±140	
L157	g–bi–pl–Kfs–sill–q–H_2O	17.0	490±280		640±60	

Sample numbers with the prefix LG are samples collected for this study, samples prefixed by L are from McFarlane (1995), samples SSM8, SRM4, SLM2, LM201 are from Inger & Harris (1992). Sample numbers shown in bold are those used in Δ*PT* calculations (see text for discussion). bi, biotite; chl, chlorite; crd, cordierite; g, garnet; ilm, ilmenite; Kfs, K-feldspar; ky, kyanite; mu, muscovite; pl, plagioclase; q, quartz; ru, rutile; sill, sillimanite; st, staurolite.

uncertainties on individual pressure estimations are typically greater than ±200 MPa (2σ), leading to the relatively large uncertainty on the gradient, and potentially also obscuring variation in the pressure gradient within the section. Pressures from MCT-zone samples plot at slightly lower pressure than samples from the HHC, but overlap within uncertainty.

RELATIVE THERMOBAROMETRY

There are a number of sources of uncertainty which contribute to the final precision of thermobarometric calculations. The most significant of these which can be treated statistically are as follows.

1 Analytical precision: uncertainties stemming from the analysis of mineral compositions via electron probe microanalyses.

2 Thermodynamic data: uncertainties associated with thermodynamic data, i.e. the calibration of barometers and thermometers or, as in the case of the Holland and Powell dataset, the enthalpies of formation of the mineral end-members (Holland & Powell, 1998).

3 Activity–composition relationships: uncertainties associated with the solution models used to calculate end-member activities from the measured mineral compositions.

In addition to these sources, there is a potentially significant contribution associated with the geological interpretation of equilibrium mineral assemblages and the selection of appropriate mineral compositions. It is difficult to treat such geological precision in a meaningful statistical manner (Kohn & Spear, 1991; Worley & Powell, 2000); however, its effect can be minimized by careful, systematic petrological observations and, specifically, X-ray compositional mapping.

Statistical treatment of the input uncertainties, outlined above, results in relatively large uncertainties on the calculated values of pressure and temperature. For example, 2σ uncertainties on *P–T* results from the Langtang section are generally greater than ±200 MPa and ±50 °C. However, recognition that many of the input uncertainties are systematic when applied to multiple samples with the same mineral assemblage has led to the recent development of a high-precision relative thermobarometry technique, termed the Δ*PT* approach (Worley & Powell, 2000). The systematic uncertainties result in calculated pressures and temperatures that are strongly correlated and therefore, although absolute *P–T* estimates may be quite uncertain, differences in *P–T* can be constrained with much more precision.

The nature of the Δ*PT* methodology is such that

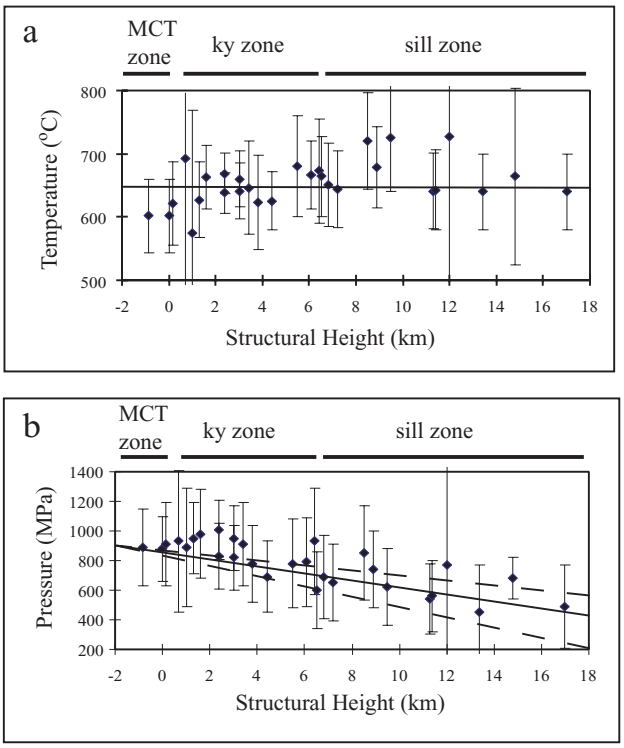

Fig. 7. Results of THERMOCALC average *P–T* calculations plotted against structural height. Error bars are 2σ. Arrows on some error bars indicate that the error limits extend beyond the temperature range of the diagram. Temperatures throughout the section plot within error of 650 °C, while pressures throughout the section plot within error of an average lithostatic gradient of 0.27 kbar km^{-1} (bold line). Also plotted are pressure gradients which are *c.* 30% steeper and shallower than lithostatic (broken lines), both of which still easily fit within error limits of the data, illustrating how much uncertainty exists in the trend defined by these data.

the highest degree of precision is achieved when applied to samples with the same mineral assemblage or subassemblage. Of the 29 samples used for THERMOCALC *P–T* calculations, 15 that contain the assemblage garnet–plagioclase–aluminosilicate–biotite–muscovite–quartz were selected for treatment with the ΔPT method (Table 3). Of these 15 samples, nine were collected for this study, five are from Macfarlane (1995), and one is from Inger & Harris (1992).

Results are shown in Fig. 8 as pressure and temperature arrays. In each case, sample LG15 from near the base of the section was chosen as an anchor point for which absolute *P–T* conditions have been calculated. The pressure and temperature of the remaining samples have been calculated as *P–T* differences relative to this anchor point (Table 3) and then scaled by the absolute *P–T* conditions as calculated for LG15. It should be noted that the *P–T* conditions calculated for LG15 using the fluid-absent subassemblage (Table 3) are slightly different from the values given in Table 2.

The ΔPT results for temperature are consistent with the average *P–T* calculations, in that they yield an essentially isothermal distribution up the structural section. The absolute values of temperature are lower by about 50 °C than those plotted in Fig. 7(a) due to the use of the fluid-absent subassemblage for ΔPT calculations. All but two of the samples give ΔPT results within uncertainty of 600 °C. Using the observation that the section is essentially isothermal allows the pressure array to be calculated by fixing $\Delta T = 0$, i.e. $T = 600$ °C for all samples, and calculating ΔP using average *P* rather than average *P–T* (Worley & Powell, 2000). This method further improves the precision on the individual ΔP results, with uncertainties reduced by a factor of at least four compared with the traditional average *P–T* approach. The $\Delta P|_{\Delta T=0}$ array reveals significant internal structure which is obscured by the relatively large uncertainties on the THERMOCALC average *P–T* results. Distinct trends in pressure with structural height emerge for the kyanite zone versus the sillimanite zone. Pressure decreases with structural height from around 900 MPa at the base of the section to around 650 MPa near the top of the kyanite zone. The trend of decreasing pressure with structural height does not continue smoothly up the section; instead, the data from the middle part of the section define a second pressure array which is displaced up-pressure compared with the samples lower in the section (Fig. 8). This trend in the middle part of the section is in turn displaced to higher pressures in the upper part of the measured section. The ΔP data therefore define a preserved pressure gradient in three segments, each of which is steeper than an average lithostatic gradient of *c.* 27 MPa km^{-1}. The total pressure variation up the section is on the order of 500 MPa, which is consistent with the conventional THERMOCALC data (Fig. 7) and the results of Macfarlane (1995). However, the apparent discontinuities in the pressure array are obscured by the large uncertainties on individual pressure determinations using the traditional approaches.

It should be noted that, although the data presented in Fig. 6 do not reveal large differences in core and rim estimates for most samples, the possibility remains that the results reflect some degree of diffusional re-equilibration subsequent to the metamorphic peak. It is well known that temperature estimates are more susceptible to diffusional re-equilibration than pressure estimates, and thus our reported temperatures may be somewhat underestimated. In the absence of an independent method for retrieving reliable temperature estimates, there is little that can be done to quantify this effect. However, the most interesting result from the ΔPT data is the discontinuous nature of the pressure array, which is unlikely to be an artifact of diffusional re-equilibration.

One obvious question raised by the ΔP array is: why do rocks from the lower half of the sillimanite zone contain sillimanite, despite preserving pressures

Table 3. Results from ΔPT calculations, using the assemblage g–bi–mu–pl–als–q, presented as temperatures and pressures relative to sample LG15. Uncertainties are 2σ.

Sample	Structural height (km)	T from average PT (°C)	P from average PT (MPa)	Average $P_{T=600\,°C}$ (MPa)
LG37	1.6	724±42	1003±80	860±50
LG35	2.4	626±31	930±60	890±30
LG36	2.4	621±39	850±70	820±40
LG15	3.0	613	880	870
L71a	3.0	594±34	770±60	770±30
L22	4.4	557±45	600±70	650±40
L25	6.1	564±39	640±70	690±50
SSM8	6.4	618±73	690±100	670±40
LG23	6.5	568±50	480±70	510±40
L26	6.8	531±55	560±80	650±40
L171	7.2	610±62	600±90	580±50
LG26	8.5	603±61	710±90	700±40
LG28	8.9	660±70	730±100	660±40
LG29	11.3	630±88	520±100	490±40
LG31	11.4	704±105	580±110	460±40

which are equivalent to those preserved by kyanite-bearing rocks immediately below? On a pressure versus temperature diagram (Fig. 9), the data, within uncertainty, plot on the correct sides of the kyanite to sillimanite boundary, resolving this apparent paradox.

In summary, the most distinctive features of the ΔPT data for the HHC at Langtang are the essentially isothermal temperature array, the discontinuities in pressure with structural height and the steeper than lithostatic pressure gradients within individual segments of the pressure array.

INTERPRETATION OF THE TEMPERATURE AND PRESSURE ARRAYS

The THERMOCALC average P–T results from the compiled dataset presented here (Fig. 7) accord with Macfarlane's (1995) data, and based on these results alone we would also have been led to fit an approximately lithostatic gradient through the entire section. In this case, we would see no compelling reason to suggest a structural break between the kyanite and sillimanite zones. However, the more detailed trends revealed by the ΔPT approach (Fig. 8) serve to illustrate the considerable uncertainties that must be attached to trends in conventional P–T data, where the precision on individual P–T estimates is relatively poor.

The most obvious explanation for the discontinuities in the pressure array revealed by the ΔPT results is tectonic juxtaposition subsequent to metamorphism. This possibility is consistent with the suggestion of Reddy *et al.* (1993) that there is a cryptic thrust between the kyanite and sillimanite zones, although our data suggest the presence of two thrust planes. No clear field evidence was found for discrete thrusts at the positions identified in the pressure array, although this is not surprising given the discontinuous nature of the outcrop and heavily wooded hillsides in the region of the kyanite to sillimanite transition. Each of the two discontinuities in the pressure array is *c.* 100 MPa, suggesting relative vertical movement of *c.* 3 km. Other features of the data presented here are the relatively steep pressure gradients within both the kyanite and sillimanite zones, and the isothermal temperature array.

The generation of steeper than lithostatic metamorphic pressure gradients over a thick structural section can be accomplished in more than one way. Jamieson *et al.* (1996) presented a model involving synmetamorphic ductile shear and showed that a wide variety of pressure arrays can be produced depending on the convergence rate. Variable rates of erosional exhumation across an orogen will also influence the preserved pressure array. Such a model may, at least in part, account for the steeper than lithostatic gradients observed in the Langtang data. It should be noted that, in this model, the preserved pressure array results from non-synchronous metamorphic equilibration across the section. In principle, therefore, this scenario could be tested by high-precision geochronology throughout the section. Alternatively, steeper than lithostatic pressure gradients could have been produced by post-metamorphic extension of the section, such that rocks equilibrated at structural positions which were vertically further separated than their present position in the section would indicate. This would accord with the observations of Reddy *et al.* (1993) who identified local areas where shear criteria in the regional foliation indicated local NE-directed extension. These zones contained sillimanite, indicating that extension took place at relatively high temperatures. The magnitude of extension required to explain the Langtang data cannot be tightly constrained, but the pressure gradients within both the kyanite and sillimanite zones are approximately double an average lithostatic gradient, as shown in Fig. 8, which would suggest extension by a factor of about two. It is possible that both synmetamorphic shearing, as in the model of Jamieson *et al.* (1996), and post-metamorphic extension have contributed to the steeper than lithostatic pressure gradients seen in the ΔPT data.

Preservation of an isothermal temperature array

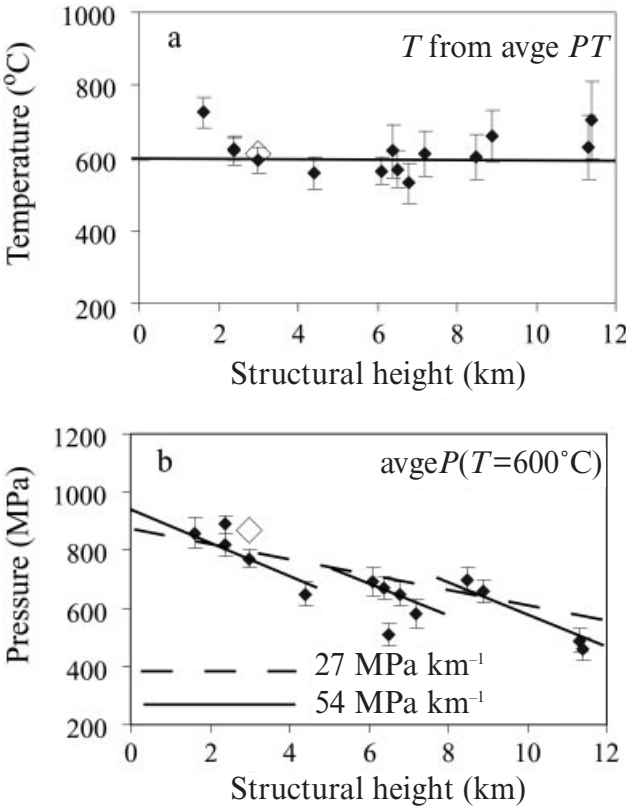

Fig. 8. Results of ΔPT calculations plotted against structural height. Error bars are 2σ and are significantly reduced when compared with the THERMOCALC results plotted in Fig. 6. In both the temperature (a) and pressure (b) arrays, sample LG15 (shown by open diamond) has been chosen as an anchor point against which the pressure and temperature of all other samples are plotted. Apart from two samples, temperatures all plot within error of 600 °C, confirming the isothermal nature of the section seen in Fig. 6(a). The pressure array shown in (b) has therefore been calculated using the ΔP approach, where ΔT is set to zero, yielding considerably reduced uncertainties (see Table 3). The pressure array exhibits structure which is obscured by the larger uncertainties on the THERMOCALC data (Fig. 6). The pressure gradient within both the kyanite zone and sillimanite zone is steeper than lithostatic, but is offset across the transition between the zones. An average lithostatic gradient (broken line) and a gradient twice lithostatic (bold line) are plotted for reference.

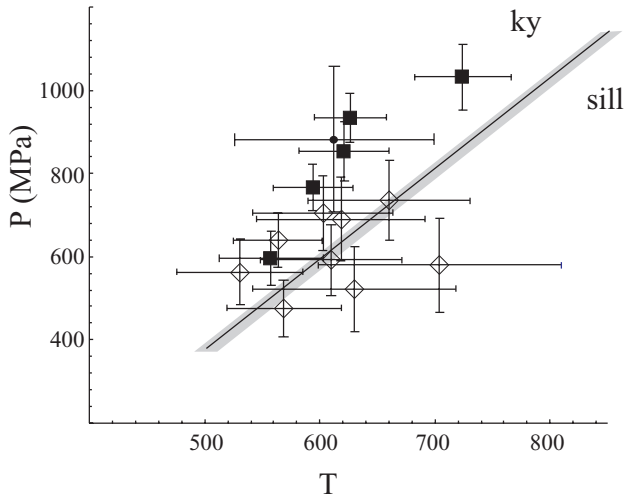

Fig. 9. ΔPT results plotted relative to the kyanite to sillimanite transition. All data points have been positioned in P–T space relative to THERMOCALC average P–T results from sample LG15, given by the filled circle with large error bars. Kyanite-zone and sillimanite-zone samples are shown by filled squares and open diamonds respectively. Note that the position of all points can shift by the amount given by the error bars on the anchor point, LG15, and that, taking this into account, all samples plot within uncertainty on the correct side of the kyanite to sillimanite transition.

spanning a range in pressure from *c*. 900 to *c*. 500 MPa suggests that peak metamorphic conditions were virtually isothermal over a depth range of about 13 km. Taken at face value, these data would therefore require an efficient heat transport mechanism in order to equalize temperatures through the section. However, we do not have convincing evidence that peak metamorphic conditions were reached synchronously throughout the section. It is likely that the timing of peak metamorphism varied both within apparently coherent parts of the section, and between different parts (e.g. Macfarlane, 1995; Jamieson *et al*., 1996).

Despite our best efforts, some uncertainty still exists in any comparative thermobarometric study such as this. The implicit assumption in our interpretation of the data is that equilibration of garnet in rocks throughout the section is systematic (although not necessarily synchronous), and therefore reveals features of the underlying thermal and baric history. The alternative is that equilibration in different parts of the section is dominated by subtle variations in rock bulk composition and cannot be interpreted in terms of regional thermal and baric structure. Such a problem is general in thermobarometry and, although it cannot be entirely discounted, the systematic variations in apparent P and T are consistent with regional P–T control on equilibration. Some of the high-frequency scatter in the data, however, may be a result of more subtle bulk compositional effects.

DISCUSSION

Two proposed zones of inverted metamorphic temperature have been identified in the Himalayas. The first is in the footwall of the MCT, where metamorphic grade in the Lesser Himalayan sequence increases up-section towards the MCT, and the second is within the hanging wall of the MCT, where sillimanite-bearing rocks overlie kyanite-bearing rocks. The origin of these apparently 'inverted' metamorphic sequences in the High Himalayas has been the subject of considerable research, resulting in the proposal of several contrasting models (e.g. Le Fort, 1975; Jaupart & Provost, 1985; Treloar *et al*., 1989; Swapp & Hollister, 1991; England *et al*., 1992; England & Molnar, 1993; Hubbard, 1996;

Jamieson *et al*., 1996). Hubbard (1996) has divided these models loosely into two categories:

1 models which invoke a heat source above the region of inverted metamorphism;

2 models which invoke post-metamorphic structural processes which invert a pre-existing right-way-up metamorphic sequence.

Type 1 models are based on the premise that the preserved metamorphic array represents a subsequently undisturbed structural section, and thus reflects the nature of the thermal regime at the time of metamorphism, while not precluding the possibility of variation in the timing of peak metamorphism within the section. Proponents of type 1 models have invoked various heat sources to account for inverted metamorphic gradients, including advection of heat within an overthrust hanging wall (Le Fort, 1975), shear heating during synmetamorphic ductile deformation (England *et al*., 1992; England & Molnar, 1993), and heat focusing by overlying low thermal conductivity Tethyan sediments (Jaupart & Provost, 1985; Inger & Harris, 1992). In contrast, proponents of type 2 models have argued that the present metamorphic character of the Himalayas is a result of post-metamorphic structural juxaposition of rocks of different grade, and potentially of different metamorphic age (Treloar *et al*., 1989; Swapp & Hollister, 1991; Hubbard, 1996).

We do not have ΔPT data to constrain the inverted metamorphism within the Lesser Himalayan sequence. However, an inverted metamorphic field gradient across the MCT is suggested by the presence of chloritoid in lower MCT-zone rocks, implying temperatures $<600\,^{\circ}C$ (e.g. Mahar *et al*., 1997), contrasting with temperatures $>600\,^{\circ}C$ within the HHC. The characteristically different zonation patterns in garnet porphyroblasts from the base of the MCT zone also suggest a distinct P–T history for these rocks. This is consistent with the recent geochronological results of Harrison *et al*. (1997) from the region immediately west of the Langtang area, indicating that metamorphism in the Lesser Himalayas is late Miocene in age (*c*. 6 Ma) compared with early Miocene (*c*. 20 Ma) metamorphism in the HHC. A detailed geochronological study would be required to assess whether metamorphism is similarly diachronous across the MCT zone in the Langtang region.

The data presented here bear on the origin of the apparent 'inverted' metamorphic sequence within the hanging wall of the MCT. The ΔPT data suggest that the Langtang section of the HHC consists of three structural blocks which were juxtaposed by post-metamorphic thrusting. The steeper than lithostatic apparent pressure gradients within the individual thrust blocks are consistent with considerable extensional deformation subsequent to metamorphism, although this effect may also have resulted from synmetamorphic deformation. We therefore do not regard the Langtang section as a structurally undisturbed section. Evidence for post-metamorphic structural disruption is not limited to the Langtang region, but has been reported in other sections through the HHC. For example, England & Molnar (1993) pointed out that the P–T data of Hubbard (1989) for the Everest region of the HHC imply structural thinning post-dating metamorphism, since the data span a range of pressures corresponding to about three times the present structural thickness of the transect. Davidson *et al*. (1997) mapped an out-of-sequence thrust, the Kakhtang thrust, in the middle of the HHC in Bhutan, which had earlier been proposed by Swapp & Hollister (1991) based on petrological observations. Treloar *et al*. (1989) described the inverted metamorphic sequence in northern Pakistan as a result of post-metamorphic thrusting.

Recognition of the tectonic juxaposition of rocks within the Langtang section raises the possibility that the different thrust sheets may represent different protoliths and/or have experienced distinct tectonothermal histories. With respect to protoliths, Parrish & Hodges (1996) reported similar Nd isotope signatures from three kyanite-zone samples and one sillimanite-zone sample. Existing geochronological data constraining the metamorphic age within the Langtang section are sparse (Parrish *et al*., 1992), and are not sufficient to test the possibility of age variations. More rigorous testing of the timing of peak metamorphism across the section will require careful comparative geochronology using both kyanite-zone and sillimanite-zone samples. This would be best attempted using monazite U–Th–Pb geochronology in a similar fashion to the work of Harrison *et al*. (1997). Contrasting ages from the kyanite and sillimanite zones would lend strong support to the interpretation of post-metamorphic structural juxtaposition.

Despite having experienced contraction, and possible extension, since metamorphism, the Langtang section shows no clear gradients or discontinuities in temperature up the section. Rather than being inverted, the metamorphic field gradient within the HHC at Langtang is essentially isothermal, relieving the need for a localized heat source in the upper part of the section, but leaving the question of how uniform peak temperatures were produced over a depth range of between 10 and 15 km.

Macfarlane (1995) preferred the explanation of Ruppel & Hodges (1994), in which rocks within the hanging wall of a thrust reach peak temperatures at different times at different structural levels, with peak temperatures falling within a range of 80–200 °C over about 15 km. She argued that the uncertainties on metamorphic temperature allow for an unrecognized temperature gradient of this magnitude. However, the more precise ΔPT data presented here place tighter constraints on relative metamorphic temperatures, yet do not reveal the presence of a temperature gradient, despite preserved pressures spanning a range corresponding to about 13 km of crustal depth. In addition, the model of Ruppel & Hodges (1994) predicts either

lithostatic or shallower than lithostatic pressure gradients in the hanging wall, in contrast to the steeper than lithostatic gradients seen in the Langtang data.

Another potential explanation for the isothermal temperature array exists in the abundant leucogranites found in the uppermost part of the Langtang Valley and elsewhere at the top of the HHC. Sillimanite-bearing migmatites immediately below the level of emplacement are precluded as a source for the leucogranites on isotopic grounds (Inger & Harris, 1993). Instead, Inger & Harris (1993) argued for a muscovite-rich source region lower in the section. Upward migration of magma from a source region low in the section provides an obvious mechanism of efficient heat transfer, potentially contributing to the observed isothermal temperature profile. However, this explanation implicitly assumes that the preserved temperature array across the section reflects the vertical distribution of peak temperatures within the crust. The recognition of post-metamorphic thrusting within the HHC allows for the possibility that different parts of the section have experienced significant horizontal transport since metamorphism. In this case, the preserved temperature array does not necessarily approximate the vertical distribution of peak temperatures, but may instead reflect the lateral distribution of heat within the orogen.

The data presented here do not bear directly on the heat source for metamorphism, which remains a point of current debate (e.g. England & Molnar, 1993; Harris & Massey, 1994; Harrison *et al*., 1997; Hodges, 1998), but suggest that models based on the preserved metamorphic field gradient, and that consider the HHC as a single coherent section, must be considered suspect.

CONCLUSIONS

This study demonstrates the utility of the ΔPT method for situations in which relative differences are more important than absolute values of P and T. The ΔPT method is most effective where a number of samples can be collected, each containing the same metamorphic assemblage, and allows the identification of trends in P–T data which may be indistinguishable by conventional geothermobarometric means.

Using the ΔPT method, we have distinguished previously unrecognized details in the preserved pressure array from the Langtang region of Nepal, which indicate post-metamorphic structural disruption of the High Himalayan Crystalline sequence. These data cast doubt on the validity of thermal models for inverted metamorphism which are based on the interpretation of the HHC as a structurally undisturbed metamorphic sequence. Recognition of structural repetition within the HHC points to a need for more detailed metamorphic geochronology in the HHC to assess the relative timing of metamorphism through the section.

ACKNOWLEDGEMENTS

We acknowledge the support of an Australian Research Council (ARC) large grant (to M. Sandiford). Dr B. N. Upreti of Tribhuvan University, Kathmandu, provided encouragement and bureaucratic help in Kathmandu. A. Camacho is thanked for assistance and discussion during fieldwork in Langtang Valley, which was ably supported by our guide, N. Sherpa, and porter, P. Shyangiba, via Glacier Dome Trekking and Expeditions Ltd. C. Noble assisted with electron probe microanalyses. We thank M. Hubbard and B. Jamieson for thorough and constructive reviews.

REFERENCES

Brown, L. D., Zhao, W., Nelson, K. D., Hauck, M., Alsdorf, D., Ross, A., Cogan, M., Clark, M., Liu, X. & Che, J., 1996. Bright spots, structure, and magmatism in southern Tibet from INDEPTH seismic reflection profiling. *Science*, **274,** 1688–1691.

Davidson, C., Grujic, D. E., Hollister, L. S. & Schmid, S. M., 1997. Metamorphic reactions related to decompression and synkinematic intrusion of leucogranite, High Himalayan Crystallines, Bhutan. *Journal of Metamorphic Geology*, **15,** 593–612.

Denison, C., Carlson, W. D. & Ketcham, R. A., 1997. Three-dimensional quantitative textural analysis of metamorphic rocks using high-resolution computed X-ray tomography: Part I. Methods and techniques. *Journal of Metamorphic Geology*, **15,** 29–44.

England, P., Le Fort, P., Molnar, P. & Pecher, A., 1992. Heat sources for Tertiary metamorphism and anatexis in the Annapurna–Manaslu region, central Nepal. *Journal of Geophysical Research*, **97,** 2107–2128.

England, P. & Molnar, P., 1993. The interpretation of inverted metamorphic isograds using simple physical calculations. *Tectonics*, **12** (1), 145–157.

England, P. & Thompson, A. B., 1984. Pressure–temperature time paths of regional metamorphism I. Heat transfer during the evolution of regions of thickened continental crust. *Journal of Petrology*, **25,** 894–928.

Ferry, J. M. & Spear, F. S., 1978. Experimental calibration of the partitioning of Fe and Mg between garnet and biotite. *Contributions to Mineralogy and Petrology*, **66,** 113–117.

Ghent, E. D., 1976. Plagioclase–garnet–Al_2SiO_5–quartz: a potential geobarometer–geothermometer. *American Mineralogist*, **61,** 710–714.

Ghent, E. D. & Stout, M. Z., 1981. Geobarometry and geothermometry of plagioclase–biotite–garnet–muscovite assemblages. *Contributions to Mineralogy and Petrology*, **76,** 92–97.

Harris, N. & Mossey, J., 1994. Decompression and anatexis of Himalayan metapelites. *Tectonics*, **13,** 1537–1546.

Harrison, T. M., Ryerson, F. J., Le Fort, P., Lovera, O. M. & Catlos, E. J., 1997. A Late Miocene–Pliocene origin for the Central Himalayan inverted metamorphism. *Earth and Planetary Science Letters*, **146,** E1–E7.

Hodges, K. V., 1998. The thermodynamics of Himalayan orogenesis. In: *What Drives Metamorphism and Metamorphic Reactions?* (eds Treloar, P. J. & O'Brien, P. J.), pp. 7–22. Geological Society of London, Special Publication No. 138, London.

Holland, T. J. B. & Powell, R., 1990. An internally-consistent thermodynamic dataset with uncertainties and correlations: the system Na_2O–K_2O–CaO–MgO–MnO–FeO–Fe_2O_3–Al_2O_3–SiO_2–TiO_2–C–H_2–O_2. *Journal of Metamorphic Petrology*, **8,** 89–124.

Holland, T. J. B. & Powell, R., 1998. An internally consistent

thermodynamic dataset for phases of petrological interest. *Journal of Metamorphic Petrology*, **16,** 309–343.

Hubbard, M. S., 1989. Thermobarometric constraints on the thermal history of the Main Central Thrust Zone and Tibetan Slab, eastern Nepal Himalaya. *Journal of Metamorphic Petrology*, **7,** 19–30.

Hubbard, M. S., 1996. Ductile shear as a cause of inverted metamorphism: example from the Nepal Himalaya. *Journal of Geology*, **104,** 493–499.

Inger, S. & Harris, N. B. W., 1992. Tectonothermal evolution of the High Himalayan Crystalline Sequence, Langtang Valley, northern Nepal. *Journal of Metamorphic Petrology*, **10,** 439–452.

Inger, S. & Harris, N. B. W., 1993. Geochemical constraints on leucogranite magmatism in the Lantang Valley, Nepal Himalaya. *Journal of Petrology*, **34,** 345–368.

Jamieson, R. A., Beaumont, C., Hamilton, J. & Fullsack, P., 1996. Tectonic assembly of inverted metamorphic sequences. *Geology*, **24,** 839–842.

Jaupart, C. & Provost, A., 1985. Heat focussing, granite genesis and inverted metamorphic gradients in continental collision zones. *Earth and Planetary Science Letters*, **73,** 385–397.

Kohn, M. & Spear, F. S., 1991. Error propagation for barometers: 2. Application to rocks. *American Mineralogist*, **76,** 138–147.

Le Fort, P., 1975. Himalaya: the collided range. Present knowledge of the continental arc. *American Journal of Science*, **275A,** 1–44.

Macfarlane, A. M., 1993. Chronology of tectonic events in the crystalline core of the Himalaya, Langtang National Park, Central Nepal. *Tectonics*, **12,** 1004–1025.

Macfarlane, A. M., 1995. An evaluation of the inverted metamorphic gradient at Langtang National Park, Central Nepal Himalaya. *Journal of Metamorphic Geology*, **13,** 595–612.

Mahar, E. M., Baker, J. M., Powell, R., Holland, T. J. B. & Howell, N., 1997. The effect of Mn on mineral stability in metapelites. *Journal of Metamorphic Geology*, **15,** 223–238.

Metcalfe, R. P., 1993. Pressure, temperature and time constraints on metamorphism across the Main Central Thrust zone and High Himalayan Slab in the Garhwal Himalaya. In: *Himalayan Tectonics* (eds Treloar, P. J. & Searle, M. P.), pp. 485–510. Geological Society Special Publication, 74, London.

Parrish, R. R. & Hodges, K. V., 1996. Isotopic constraints on the age and provenance of the Lesser and Greater Himalayan sequences, Nepalese Himalaya. *Geological Society of America Bulletin*, **108,** 904–911.

Parrish, R. R., Hodges, K. V. & McFarlane, A. M., 1992. U–Pb geochronology of igneous and metamorphic rocks near the Main Central Thrust in the Langtang area, central Nepal Himalaya. *7th Annual Himalayan–Karakorum–Tibet Workshop, Oxford, UK, April, 1992.*

Powell, R. & Holland, T. J. B., 1988. An internally consistent thermodynamic dataset with uncertainties and correlations: 3. Application methods, worked examples and a computer program. *Journal of Metamorphic Geology*, **6,** 173–204.

Reddy, S. M., Searle, M. P. & Massey, J. A., 1993. Structural evolution of the High Himalayan Gneiss sequence, Langtang Valley, Nepal. In: *Himalayan Tectonics* (eds Treloar, P. J. & Searle, M. P.), pp. 375–389. Geological Society Special Publication, 74, London.

Ruppel, C. & Hodges, K. V., 1994. Pressure–temperature–time paths from two-dimensional thermal models: prograde, retrograde, and inverted metamorphism. *Tectonics*, **13** (1)**,** 17–44.

Spear, F. S., 1993. *Metamorphic Phase Equilibria and Pressure–Temperature–Time Paths.* Mineralogical Society of America Monograph, Washington.

Swapp, S. M. & Hollister, L. S., 1991. Inverted metamorphism within the Tibetan slab of Bhutan: evidence for a tectonically transported heat source. *Canadian Mineralogist*, **29,** 1019–1041.

Treloar, P. J., Broughton, R. D., Williams, M. P., Coward, M. P. & Windley, B. F., 1989. Deformation, metamorphism and imbrication of the Indian plate, south of the Main Mantle Thrust, north Pakistan. *Journal of Metamorphic Geology*, **7,** 111–125.

Vannay, J. C., Sharp, Z. D. & Graseman, B., 1999. Himalayan inverted metamorphism constrained by oxygen isotope thermometry. *Contributions to Mineralogy and Petrology*, **137,** 90–101.

Worley, B. & Powell, R., 2000. High-precision relative thermobarometry: theory and a worked example. *Journal of Metamorphic Geology*, **18,** 91–114.

Received 9 June 1999; revision accepted 12 May 2000.